Numerical Heat Transfer, Part A: Applications

ISSN: 1040-7782 (Print) 1521-0634 (Online) Journal homepage: http://www.tandfonline.com/loi/unht20

Bifurcation and Hysteresis of Flow Pattern Transition in a Shallow Molten Silicon Pool with Cz Configuration

Lan Peng , You-Rong Li , Ying-Jie Liu , Nobuyuki Imaishi , Tien-Chien Jen & Qing-Hua Chen

To cite this article: Lan Peng , You-Rong Li , Ying-Jie Liu , Nobuyuki Imaishi , Tien-Chien Jen & Qing-Hua Chen (2007) Bifurcation and Hysteresis of Flow Pattern Transition in a Shallow Molten Silicon Pool with Cz Configuration, Numerical Heat Transfer, Part A: Applications, 51:3, 211-223, DOI: 10.1080/10407780600879014

To link to this article: http://dx.doi.org/10.1080/10407780600879014

Published online: 13 Feb 2007.

Numerical Heat Transfer, Part A, 51: 211–223, 2007

ISSN: 1040-7782 print/1521-0634 online
DOI: 10.1080/10407780600879014

Taylor & Francis
Taylor & Francis Group

BIFURCATION AND HYSTERESIS OF FLOW PATTERN TRANSITION IN A SHALLOW MOLTEN SILICON POOL WITH Cz CONFIGURATION

Lan Peng, You-Rong Li, and Ying-Jie Liu
College of Power Engineering, Chongqing University, Chongqing, People's Republic of China

Nobuyuki Imaishi
Institute for Materials Chemistry and Engineering, Kyushu University, Fukuoka, Japan

Tien-Chien Jen and Qing-Hua Chen
Mechanical Engineering Department, University of Wisconsin, Milwaukee, Wisconsin, USA

Three-dimensional numerical simulations of transient thermal convection in a shallow molten silicon pool with Czochralski configuration (depth $d = 3$ mm) have been conducted to understand the transition mechanism of the flow patterns on silicon melt in Czochralski furnaces. The crucible side wall is maintained at constant temperature. Bottom and free surfaces are either adiabatic or allow heat transfer in the vertical direction. The simulation results indicate that two flow transitions occur when the radial temperature difference along the free surface increases. First, the steady two-dimensional flow becomes steady three-dimensional flow, and then it evolves to three-dimensional oscillatory flow when the temperature difference is further increased. This oscillatory flow is characterized by spoke patterns traveling in either the clockwise or counterclockwise direction. It is observed that a transition hysteresis exists from oscillatory three-dimensional flow to steady three-dimensional flow when the radial temperature difference decreases. The critical conditions for the flow pattern transition are determined. Characteristics of the bifurcation and hysteresis of flow pattern transition are discussed.

1. INTRODUCTION

The Czochralski (Cz) method is one of the most important methods of producing silicon single crystals from the melt. In this method, the buoyancy and thermocapillary forces are coupled to cause the melt convection in the crucible. In the past

Received 19 February 2006; accepted 3 June 2006.

This work was partly supported by the NSFC (grant number 50476042) and partly by the Scientific Research Foundation for the Returned Overseas Chinese Scholars, State Education Ministry of China. Dr. Tien-Chien Jen and Mr. Qinghua Chen would also like to acknowledge the partial financial support of National Science Foundation through DMI 9908324.

Address correspondence to You-Rong Li, College of Power Engineering, Chongqing University, Chongqing 400044, People's Republic of China. E-mail: liyourong@cqu.edu.cn

NOMENCLATURE

A	amplitude of temperature oscillation, K	λ	thermal conductivity, W/m K
c_p	heat capacity, J/kg K	μ	dynamic viscosity, kg/m s
d	depth, m	ν	kinematic viscosity, m^2/s
$\mathbf{e}_z$	z-directional unit vector	ρ	density of the melt, kg/m^3
g	gravitational acceleration, m/s^2	ρ_T	thermal expansion coefficient of the melt, K^{-1}
m	azimuthal wave number	σ	Stefan-Boltzmann constant, $W/m^2 K^4$
p	pressure, Pa	ω	angular velocity of hydrothermal waves, rad/s
Pr	Prandtl number ($= \nu/\alpha$)		
q	heat flux, W/m^2	**Subscripts**	
r	radius, m	a	ambient
t	time, s	c	crucible
T	temperature, K	cri	critical
$\mathbf{v}$	velocity vector	h	heated
z	axial coordinate, m	m	melting point
α	thermal diffusivity, m^2/s	r	radial
γ_T	temperature coefficient of surface tension, N/m K	s	crystal
ε	emissivity of the melt	z	axial
θ	azimuthal coordinate, rad	θ	azimuthal

few decades, thermocapillary convection has received much attention from both fundamental and applied aspects, especially in microgravity-related fluid mechanics and in semiconductor single-crystal growth from melt. Smith and Davis [1] performed a linear stability analysis of a thin and infinitely extended fluid layer with a free upper surface subjected to a constant horizontal temperature gradient. They found two types of three-dimensional instabilities, i.e., stationary longitudinal rolls and oblique hydrothermal waves, depending on the Prandtl (Pr) number and basic flow pattern (with or without a return flow), and determined the critical Marangoni number. They also predicted that there would exist bifurcation of the flow pattern transition. Subsequently, Laure and Roux [2] extended Smith and Davis's work to account for the influence of buoyancy forces for low-Pr fluids. Meanwhile, Yamagishi and Fusegawa [3] performed an experimental study of thermocapillary-buoyancy flow and observed dark lines at the surface of the melt by CCD camera during silicon Cz growth. Since this pattern looks like the spoke of a wheel, it is called a spoke pattern. Furthermore, Nakamura [4] observed the thermal waves due to a nonaxisymmetric flow at a Czochralski-type silicon-melt surface with a carbon-dummy crystal when the crucible rotates. It was found that the thermal wave number increased with increase of the crucible rotation rate and that the traveling rate of the thermal wave in the azimuthal direction was slower than the crucible rotation rate. Recently, Azami et al. [5] observed the moving spoke patterns on the free surface of a shallow pool of high-temperature silicon melt (3 mm and 8 mm in depth) and reported that thermocapillary flow may play an important role in the incipience of the three-dimensional (3-D) convection and the number of spokes.

It is difficult to understand the details of transient thermal convection in a shallow molten silicon pool with Czochralski configuration through experiments.

Recent developments in computers allow us to conduct large-scale, 3-D, nonsteady, numerical simulations [6–17]. Yi et al. [18] performed a 3-D numerical simulation of the silicon melt flow and verified asymmetric temperature profiles similar to the spoke patterns. They concluded that the Rayleigh-Benard or Marangoni-Benard instability (or both) can cause spoke patterns in the silicon melt. Li et al. [19, 20] conducted a series of unsteady 3-D numerical simulations of thermocapillary and thermocapillary-buoyancy flows of silicon melt in a shallow annular pool heated from the outer wall and cooled at the inner cylindrical wall and verified the existence of the hydrothermal waves. In our previous articles [21, 22], comprehensive numerical simulations of the thermocapillary and thermocapillary-buoyancy flow in a shallow pool of silicon melt which is heated from the outer wall and cooled at the cylindrical inner rod which touches the surface of the melt just like the Cz configuration were performed. The geometry configuration is exactly the same as that of the experimental apparatus of Azami et al. [5]. It was found that two flow transitions occur when the radial temperature difference along the free surface is increased. First, the steady two-dimensional (2-D) flow becomes steady 3-D flow, and then it evolves to oscillatory 3-D flow when the temperature difference is further increased. In the present study, numerical simulations on the characteristics of the bifurcation and hysteresis of flow pattern transition in a shallow pool of silicon melt are reported.

2. MODEL FORMULATION

2.1. Basic Assumptions and Governing Equations

The thermocapillary flow (hereafter we denote this as the Ma-driven flow) in a shallow molten silicon pool with Cz configuration as shown schematically in Figure 1 is analyzed. Furthermore, when the buoyancy force is taken into consideration, it is denoted as the Ma + B-driven flow. The radius of the cylindrical rod (hereafter we call this the "crystal") is $r_s = 15\,\text{mm}$, the crucible radius $r_c = 50\,\text{mm}$, and the depth is $d = 3\,\text{mm}$. The melt/crystal interface and crucible side wall are maintained at constant temperatures T_m and $T_h > T_m$, respectively. T_m (=1,683 K) is the melting-point temperature of silicon. The following assumptions are introduced in our model.

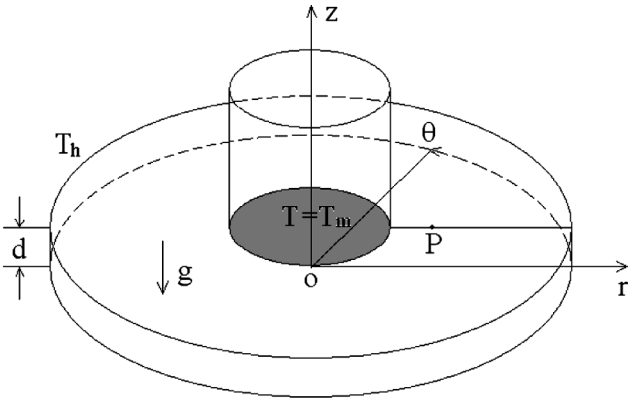

Figure 1. Configuration of the system.

1. Silicon melt is an incompressible Newtonian fluid that satisfies the Boussinessq approximation except for the surface tension.
2. The velocity is small and the flow is laminar.
3. The upper surface is flat and nondeformable.
4. At the free surface, the thermocapillary force is taken into account.
5. On every solid–liquid boundary, the no-slip condition is applied.

In order to evaluate the effect of vertical heat flux, two types of thermal boundary conditions on the free and bottom surfaces were introduced:

Case A: adiabatic on the free and bottom surfaces
Case B: heated at the bottom surface with a constant heat flux ($q = 3\,\mathrm{W/cm^2}$) and radiative heat loss to the ambient at an effective temperature $T_a = 1{,}599\,\mathrm{K}$ from the free surface

The thermophysical properties of silicon melt at $T_m = 1{,}683\,\mathrm{K}$ are listed in Table 1.

With the above assumptions, the flow and heat transfer equations are expressed as follows.

$$\nabla \cdot \mathbf{v} = 0 \tag{1}$$

$$\frac{\partial \mathrm{v}}{\partial t} + \mathbf{v} \cdot \nabla \mathbf{v} = -\frac{1}{\rho}\nabla p + \nu \nabla^2 \mathbf{v} + \rho_T g(T - T_m)\mathrm{e}_z \tag{2}$$

$$\frac{\partial T}{\partial t} + \mathbf{v} \cdot \nabla T = \alpha \nabla^2 T \tag{3}$$

The boundary conditions at the free surface ($z = d,\ r_s < r < r_c,\ 0 \le \theta < 2\pi$) are

$$\mu \frac{\partial v_r}{\partial z} = \gamma_T \frac{\partial T}{\partial r} \tag{4a}$$

$$\mu \frac{\partial v_\theta}{\partial z} = \gamma_T \frac{\partial T}{r\,\partial \theta} \tag{4b}$$

$$v_z = 0 \tag{4c}$$

Table 1. Physical properties

Symbol	Value	Unit
T_m	1,683	K
λ	64	W/m K
ρ	2,530	kg/m^3
μ	7.0×10^{-4}	kg/m s
c_p	1,000	J/kg K
ρ_T	1.5×10^{-4}	K^{-1}
γ_T	-7.0×10^{-5}	N/m K
Pr	0.011	—

$$\frac{\partial T}{\partial z} = 0 \qquad \text{or} \qquad -\lambda \frac{\partial T}{\partial z} = \varepsilon\sigma(T^4 - T_a^4) \tag{4d}$$

At the melt/crystal interface ($z = d,\ r \le r_s,\ 0 \le \theta < 2\pi$),

$$v_r = 0 \tag{5a}$$

$$v_\theta = 0 \tag{5b}$$

$$v_z = 0 \tag{5c}$$

$$T = T_m \tag{5d}$$

At the bottom ($z = 0,\ r < r_c,\ 0 \le \theta < 2\pi$),

$$v_r = 0 \tag{6a}$$

$$v_\theta = 0 \tag{6b}$$

$$v_z = 0 \tag{6c}$$

$$\frac{\partial T}{\partial z} = 0 \qquad \text{or} \qquad -\lambda \frac{\partial T}{\partial z} = q \tag{6d}$$

At the crucible side wall ($r = r_c,\ 0 \le z \le d,\ 0 \le \theta < 2\pi$),

$$v_r = 0 \tag{7a}$$

$$v_\theta = 0 \tag{7b}$$

$$v_z = 0 \tag{7c}$$

$$T = T_h \tag{7d}$$

At the beginning, since the radial temperature difference along the free surface is very small, the following initial conditions ($t = 0$) are used:

$$v_r = 0 \tag{8a}$$

$$v_\theta = 0 \tag{8b}$$

$$v_z = 0 \tag{8c}$$

$$T = T_m \qquad r \le r_s \tag{8d}$$

$$T = T_h - (T_h - T_m)\frac{\ln(r/r_c)}{\ln(r_s/r_c)} \qquad r > r_s \tag{8e}$$

However, in order to reduce computational effort, the result of a small ΔT is used as initial condition when ΔT is increased, and the result of a large ΔT is used as the initial condition when ΔT is decreased.

2.2. Numerical Method

The fundamental equations are discretized by the finite-volume method. The modified central difference approximation is applied to the diffusion terms, while the QUICK scheme is used for the convective terms. The SIMPLER algorithm [23] is used to handle the pressure–velocity coupling. In this study, nonuniform staggered grids of $62^r \times 22^z \times 60^\theta$ are used. The validation of the code for the thermocapillary and thermocapillary-buoyancy flow simulation was performed in our previous works [19–22] and will not be repeated here.

Numerical simulations were conducted on an MPU of the Fujitsu VPP700 at the Computer Center of Kyushu University. The time increment was chosen between 0.5×10^{-3} and 5×10^{-3} s. Convergence at each time step was assumed if the maximum residual error of the continuity equation among all control volumes became less than $10^{-5}\,s^{-1}$.

3. RESULTS AND DISCUSSION

Any radial temperature difference ($\Delta T = T_h - T_m > 0$) produces a surface tension gradient on the free surface of the melt combined with the Marangoni effect with the buoyancy-induced flow in the melt layer. In the present case, surface fluid flows from the crucible side wall toward the crystal and recirculation flow exists near the bottom. The flow below the crystal is weak. If the temperature gradient is small, the flow is steady and axisymmetric. This type of flow is called the basic flow (BF). However, when the temperature gradient is increased, two flow transitions occur. First, the steady 2-D flow becomes steady 3-D flow (stationary roll, which is denoted as SR), and then it becomes oscillatory 3-D flow (hydrothermal wave, which is denoted as HTW) [21, 22]. During the second transition, bifurcation and hysteresis of flow pattern occur and will be discussed in the following sections.

3.1. Bifurcation of the Second Flow Pattern Transition

When ΔT exceeds the second critical value $\Delta T_{\mathrm{cri2,max}}$, 3-D disturbances are initiated and their amplitudes increase with time. Finally, a 3-D oscillatory flow pattern is established [21, 22]. In order to obtain all possible solutions of the 3-D oscillatory flow and save computational time, the result of a steady 3-D flow slightly below the second critical value was used as the initial conditions. The time increment between 0.5×10^{-3} and 5×10^{-3} s was used when $\Delta T > \Delta T_{\mathrm{cri2}}$. It was found that there are two group oscillatory flow and temperature fields with different propagation directions. Figure 2 shows the propagating angular velocity ω of oscillatory flow as a function of ΔT.

Here, the surface temperature fluctuation δT is introduced in order to extract the 3-D disturbances. This fluctuation δT is defined as

$$\delta T(r, \theta, z, t) = T(r, \theta, z, t) - \frac{1}{2\pi}\int_0^{2\pi} T(r, \theta, z, t)\, d\theta \tag{9}$$

In the oscillatory flow region, many traveling curved spoke patterns are observed on the entire surface. These correspond to the "hydrothermal wave"

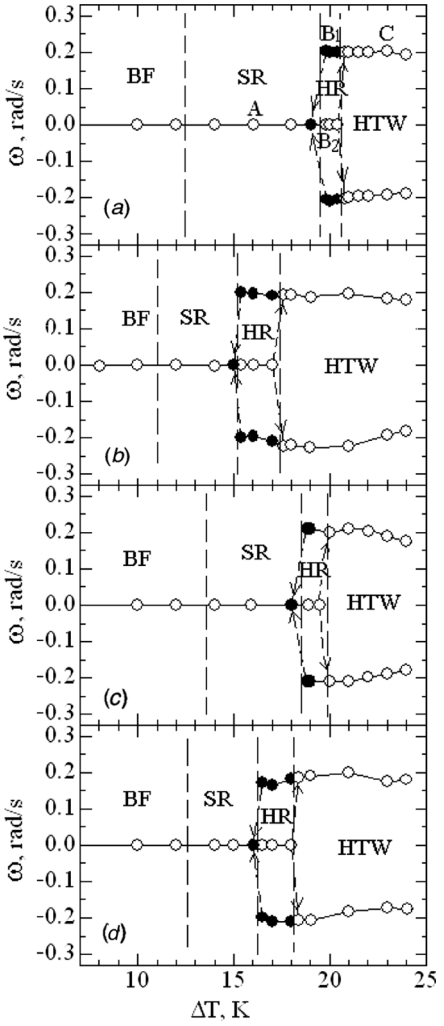

Figure 2. Bifurcation diagram. (*a*) Ma-driven for case A. (*b*) Ma + B-driven for case A. (*c*) Ma-driven for case B. (*d*) Ma + B-driven for case B. BF, basic flow; SR, stationary roll; HR, hysteresis region; HTW, hydrothermal wave. ○, increasing ΔT; ●, decreasing ΔT.

(HTW) instability. For example, at $\Delta T = 22\,\mathrm{K}$, as shown in Figure 3 for Ma-driven flow, there are the two possible traveling waves moving along different propagation directions. In Figure 3*a*, five hot (dark) and five cold (bright) spots of comparable intensity indicate the mode (number of waves) $m = 5$. In this case, the hydrothermal wave is propagating in the counterclockwise direction with the number of spokes $m = 5$. In Figure 3*b*, it is interesting to see that the hydrothermal wave is propagating in the clockwise direction with the number of spokes also 5. The angles (ϕ) between wave propagation and radial direction, measured at $r = 25\,\mathrm{mm}$, are about 75–80° and 100–105°, respectively, which is close to the angle values predicted by the linear stability theory for an infinite rectangular layer [1]. However, as seen from Figure 3,

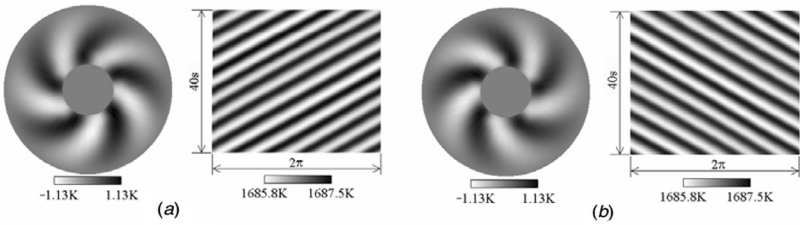

Figure 3. Snapshots of surface temperature (left) and space–time diagram of surface temperature distribution at $r = 20\,\text{mm}$ (right) at $\Delta T = 22\,\text{K}$ for case A, Ma-driven. (*a*) HTW propagating in the counterclockwise direction. (*b*) HTW propagating in the clockwise direction.

the spokes are not straight but bent. Therefore, these hydrothermal traveling waves result in many parallel tilted straight lines on the space–time diagram (STD) taken at $r = 20\,\text{mm}$ (Figure 3).

The circumferential view of the temperature distribution and the flow structure at $r = 25\,\text{mm}$ and $t = 150\,\text{s}$ is shown in Figure 4 for case A (Ma-driven flow) at $\Delta T = 22\,\text{K}$. In this case, the shallow molten silicon pool is occupied by hydrothermal waves in both cases. It is worth noting that $|v_\theta(+)| > |v_\theta(-)|$ when hydrothermal waves propagate in the counterclockwise direction (Figure 4*a*). On the contrary, $|v_\theta(+)| < |v_\theta(-)|$ when hydrothermal waves propagate in the clockwise direction (Figure 4*b*). As indicated by Smith and Davis [1] and by Levenstam and Amberg [24], the hydrothermal waves are maintained by the coupling of temperature and velocity disturbances in the melt pool.

To recognize the propagating direction of HTWs established in the melt, a net azimuthal flow is calculated. The net azimuthal flow is determined by integrating the entire shallow cylinder volume, and it can be expressed as

$$v_{\theta,\text{ave}} = \frac{1}{\pi r_c^2 d} \int\int\int v_\theta(r,\ \theta,\ z,\ t) r\, dz\, dr\, d\theta \tag{10}$$

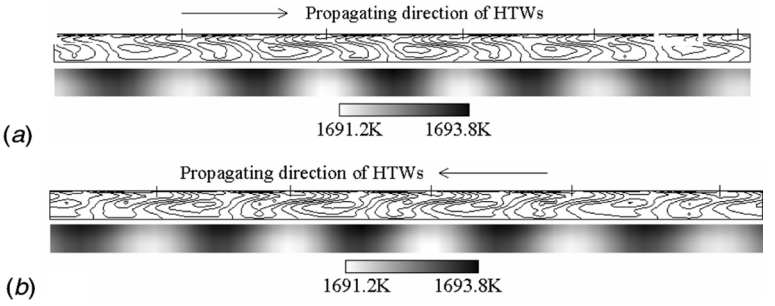

Figure 4. Circumferential view of temperature distribution and flow structure at $t = 150\,\text{s}$ and $r = 25\,\text{mm}$ for $\Delta T = 22\,\text{K}$ for case A by Ma-driven. (*a*) HTW propagating in the counterclockwise direction. $v_\theta(-) = -3.90\,\text{mm/s}$, $v_\theta(+) = 4.12\,\text{mm/s}$. (*b*) HTW propagating in the clockwise direction. $v_\theta(-) = -4.14\,\text{mm/s}$, $v_\theta(+) = 3.92\,\text{mm/s}$.

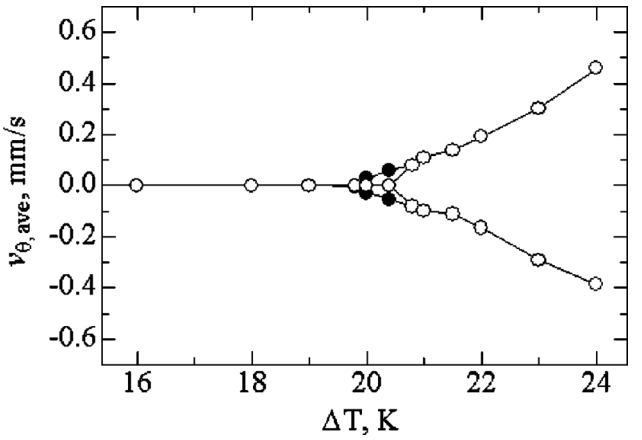

Figure 5. Net azimuthal flow for case A, Ma-driven, defined by Eq. (10), versus ΔT. ○, increasing ΔT; ●, decreasing ΔT.

The net azimuthal flow for case A by Ma-driven is shown in Figure 5. It confirms that the net azimuthal flow is zero for 2-D axisymmetric flow and for steady 3-D flow when the temperature difference is small. After the second threshold value, the net azimuthal flow starts to deviate from zero. When the net azimuthal flow is greater than zero, this results in a clockwise hydrothermal flow pattern as shown in Figure 3*b*. On the contrary, when the net azimuthal flow is less than zero, a counterclockwise hydrothermal flow pattern is formed (Figure 3*a*). All these are consistent with the angular velocity of hydrothermal wave shown in Figure 2*a*. It is also observed that the net azimuthal flow is much less sensitive to the buoyancy and thermal boundary conditions on the free and bottom surfaces, once the HTWs appear in the melt pool.

With increasing ΔT (Ma), the number of spoke patterns decreases and the amplitude of the maximum temperature oscillation (A) on the free surface increases, as shown in Figure 6. Obviously, the temperature oscillation for case A is larger than for case B. Furthermore, when the buoyancy is considered (triangular symbol), the flow is enhanced and the amplitude of the maximum temperature oscillation on the free surface is also increased.

3.2. Hysteresis of the Second Flow Pattern Transition

After the HTWs appear on the melt pool above the second critical value, the temperature difference is gradually decreased and uses the results with large ΔT as the initial conditions. It is found that the critical value $\Delta T_{\text{cri2,min}}$ of the flow transition from the HTW to SR becomes smaller than the critical value $\Delta T_{\text{cri2,max}}$ of the flow transition from the SR to HTW. This implies that there exists hysteresis for the second flow pattern transition. Note that the hysteresis temperature difference is defined as: $\delta T_{\text{cri2}} = \Delta T_{\text{cri2,max}} - \Delta T_{\text{cri2,min}}$, which is shown in Table 2. Obviously, the hysteresis temperature difference depends on the driving mechanisms and the thermal boundary conditions on the free and bottom surfaces. When

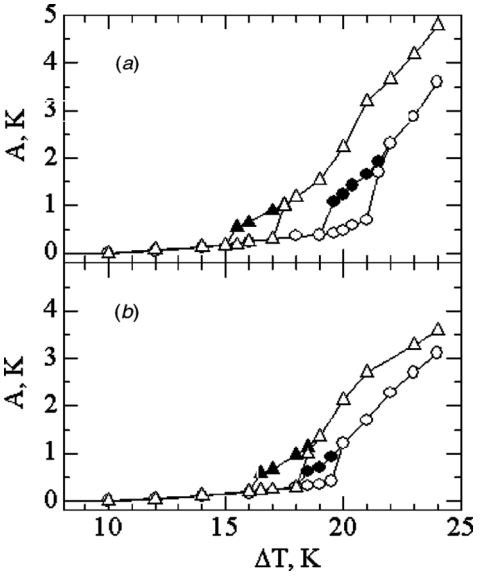

Figure 6. Variation of the maximum temperature oscillatory A on the free surface as functions of ΔT. Open symbols, increasing ΔT; filled symbols, decreasing ΔT. Circle, Ma-driven; triangle, Ma + B-driven. (*a*) case A. (*b*) case B.

buoyancy is considered Ma + B-driven flow, the flow is enhanced and the second flow pattern transition is pushing forward (at smaller ΔT_{cri2}), but the hysteresis temperature difference increases. The vertical heat transfer increases the hysteresis temperature difference for the Ma-driven flow. However, when buoyancy (B + Ma-driven flow) is considered, the hysteresis temperature is decreased.

Figure 7 illustrates an example for hysteresis of the second flow pattern transition for case A by Ma-driven flow. When the temperature difference increases to above 21 K, the flow pattern transition occurs from the stationary roll to the hydrothermal wave. However, when the temperature difference decreases to below 19 K, the flow pattern returns to the stationary roll. Figure 8 shows variation of the azimuthal velocity disturbances at monitoring point P ($r = 20$ mm, $\theta = 0$, $z = 3$ mm) mm) for case A by Ma-driven when ΔT decreases from 20 to 19 K. In this case, it was found that the transient time to establish the stationary roll from the HTW is about 55 s.

Table 2. Hysteresis temperature difference of the second flow pattern transition

Case	Driving mechanism	$\Delta T_{cri2,max}$, K	$\Delta T_{cri2,min}$, K	δT_{cri2}, K
A	Ma	20.6	19.5	1.1
	B + Ma	17.4	15.2	2.2
B	Ma	19.9	18.4	1.5
	B + Ma	18.2	16.3	1.9

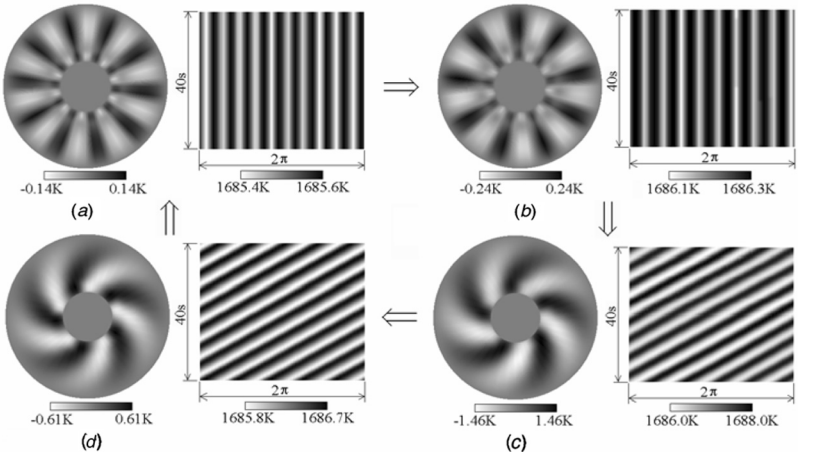

Figure 7. Hysteresis of the second flow pattern transition for case A, Ma-driven. (*a*) Point A, $\Delta T = 16\,\mathrm{K}$. (*b*) Point B_1, $\Delta T = 20\,\mathrm{K}$. (*c*) Point C, $\Delta T = 23\,\mathrm{K}$. (*d*) Point B_2, $\Delta T = 20\,\mathrm{K}$. (Points A, B_1, C, and B_2 are shown in Figure 2).

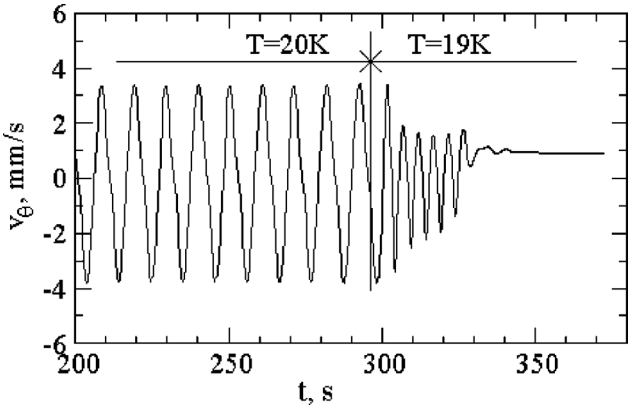

Figure 8. Variation of azimuthal velocity disturbances at monitoring point P for case A, Ma-driven, at decreasing ΔT from 20 to 19 K.

If we continue to decrease the temperature difference to below the first critical value, the flow pattern transition from the stationary roll to the stable and axisymmetric flow occurs. In this transition, however, the hysteresis does not appear.

Variations of the propagating angular velocity ω of the HTWs and the maximum temperature oscillation (A) on the free surface within the hysteresis region are shown in Figures 2 and 6, respectively. In this region, the maximum temperature oscillation of the HTWs is always larger than those of stationary rolls.

4. CONCLUSIONS

A comprehensive 3-D numerical simulations of thermocapillary and thermocapillary-buoyancy flow in a shallow silicon melt pool with the Cz configuration

(heated from the outside wall and cooled by a crystal touched to the melt surface) were conducted using the finite-volume method. From the simulation results, the following conclusions can be drawn.

1. The numerical results showed two possible types of the hydrothermal waves, with different propagation direction in the shallow silicon melt pool with the Cz configuration after the second flow pattern transition happens.
2. The bifurcation is shown in the ω–ΔT diagram. The angular velocity of the hydrothermal wave propagation depends on the driving mechanisms, the thermal boundary conditions on the free and bottom surfaces, and the temperature difference along the free surface.
3. There exists hysteresis for the second flow pattern transition. When buoyancy is considered, the hysteresis temperature difference increases. The vertical heat transfer increases the hysteresis temperature difference for the Ma-driven flow. However, when the buoyancy (B + Ma-driven flow) is considered, the hysteresis temperature is decreased.
4. When the temperature difference is increased, the maximum temperature oscillation also increases.

REFERENCES

1. M. K. Smith and S. H. Davis, Instabilities of Dynamic Thermocapillary Liquid Layers. Part 1. Convective Instabilities, *J. Fluid Mech.*, vol. 132, pp. 119–144, 1983.
2. P. Laure and B. Roux, Linear and Non-Linear Analysis of the Hadley Circulation, *J. Crystal Growth*, vol. 97, pp. 226–234, 1989.
3. H. Yamagishi and I. Fusegawa, Experimental Observation of a Surface Pattern on a Czochralski Silicon Melt, *J. Jpn. Assoc. Crystal Growth*, vol. 17, pp. 304–311, 1990.
4. S. Nakamura, M. Eguchi, T. Azami, and T. Hibiya, Thermal Waves of a Nonaxisymmetric Flow in a Czochralski-Type Silicon Melt, *J. Crystal Growth*, vol. 207, pp. 55–61, 1999.
5. T. Azami, S. Nakamura, M. Eguchi, and T. Hibiya, The Role of Surface-Tension-Driven Flow in the Formation of a Surface Pattern on a Czochralski Silicon Melt, *J. Crystal Growth*, vol. 233, pp. 99–107, 2001.
6. U. Buckle and M. Peric, Numerical Simulation of Buoyant and Thermocapillary Convection in a Square Cavity, *Numer. Heat Transfer A*, vol. 21, pp. 121–141, 1992.
7. R. Marek and J. Straub, Hybrid Relaxation—A Technique to Enhance the Rate of Convergence of Iterative Algorithms, *Numer. Heat Transfer B*, vol. 23, pp. 483–497, 1993.
8. C. W. Lan and D. T. Yang, Numerical Investigation of Heat Flow and Interfaces in the Vertical Zone—Melting Crystal Growth, *Numer. Heat Transfer A*, vol. 29, pp. 131–146, 1996.
9. M. Yao, D. H. Matthiesen, and A. Chait, Numerical Simulation of Heat Transfer and Fluid Flow in Direction Crystal Growth of GaAs, *Numer. Heat Transfer A*, vol. 30, pp. 685–701, 1996.
10. N. Kim, N. K. Anand, and D. L. Rhode, A Study on Convergence Criteria for a Simple-Based Finite-Volume Algorithm, *Numer. Heat Transfer B*, vol. 34, pp. 401–417, 1998.
11. Z. Li and B. Sonl, Fast and Accurate Numerical Approaches for Stefan Problems and Crystal Growth, *Numer. Heat Transfer B*, vol. 35, pp. 461–484, 1999.

12. A. Chatterjee, V. Prasad, and D. Sun, A Full 3-Dimensional Adaptive Finite Volume Scheme for Transport and Phase-Change Processes, Part II: Application to Crystal Growth, *Numer. Heat Transfer A*, vol. 37, pp. 823–843, 2000.
13. M. M. Rahman and T. Siikonen, A Dual-Dissipation Scheme for Pressure–Velocity Coupling, *Numer. Heat Transfer B*, vol. 42, pp. 231–242, 2002.
14. Y. R. Li, L. Peng, Y. Akiyama, and N. Imaishi, Three-Dimensional Numerical Simulation of Thermocapillary Flow of Moderate Prandtl Number Fluid in Annular Pool, *J. Crystal Growth*, vol. 259, pp. 374–387, 2003.
15. Y. R. Li, S. Y. Wu, L. Peng, and C. H. Feng, Natural Convection During Czochralski Single Crystal Growth of Super-Conducting Materials, *Mod. Phys. Lett. B*, vol. 18, pp. 1533–1536, 2004.
16. T. Morii, A New Efficient Algorithm for Solving an Incompressible Flow on Relatively Fine Mesh, *Numer. Heat Transfer B*, vol. 47, pp. 593–610, 2005.
17. V. Ginkin, Q. Naumenko, M. Zabudko, A. Kartavykh, and M. Milvidsky, Mathematical Model of Heat and Mass Transfer During Crystal Growth Process Including Cluster Model of a Melt Constitution, *Numer. Heat Transfer B*, vol. 47, pp. 459–472, 2005.
18. K.W. Yi, K. Kakimoto, M. Eguchi, M. Watanabe, T. Shyo, and T. Hibiya, Spoke Patterns on Molten Silicon in Czochralski System, *J. Crystal Growth*, vol. 144, pp. 20–28, 1994.
19. Y. R. Li, N. Imaishi, T. Azami, and T. Hibiya, Three-Dimensional Oscillatory Flow in a Thin Annular Pool of Silicon Melt, *J. Crystal Growth*, vol. 260, pp. 28–42, 2004.
20. Y. R. Li, L. Peng, S. Y. Wu, N. Imaishi, and D. L. Zeng, Thermocapillary-Buoyancy Flow of Silicon Melt in a Shallow Annular Pool, *Cryst. Res. Technol.*, vol. 39, pp. 1055–1062, 2004.
21. Y. R. Li, X. J. Quan, L. Peng, N. Imaishi, S. Y. Wu, and D. L. Zeng, Three-Dimensional Thermocapillary-Buoyancy Flow in a Shallow Molten Silicon Pool with Cz Configuration, *Int. J. Heat Mass Transfer*, vol. 48, 1952–1960, 2005.
22. Y. R. Li, N. Imaishi, L. Peng, S. Y. Wu, and T. Hibiya, Thermocapillary Flow in a Shallow Molten Silicon Pool with Czochralski Configuration, *J. Crystal Growth*, vol. 266, pp. 88–95, 2004.
23. S. V. Patankar, *Numerical Heat Transfer and Fluid Flow*, Hemisphere, New York, 1980.
24. M. Levenstam and G. Amberg, Hydrodynamical Instabilities of Thermocapillary Flow in a Half-Zone, *J. Fluid Mech.*, vol. 297, pp. 357–382, 1995.